Applied Surface Science 703 (2025) 163405

Contents lists available at ScienceDirect

Applied Surface Science

journal homepage: www.elsevier.com/locate/apsusc

Full Length Article

Microwaves assisted synthesis of IrRu alloy nanoparticles for acidic oxygen evolution reaction: A balance between activity and stability

Inayat Ali Khan [a,b], Per Morgen [a], Saso Gyergyek [c], Raghunandan Sharma [a,*], Shuang Ma Andersen [a,*]

[a] Department of Green Technology, University of Southern Denmark, Odense M 5230, Denmark
[b] Department of Chemistry, School of Natural Sciences (SNS), National University of Sciences and Technology (NUST), Islamabad 44000, Pakistan
[c] Department for Materials Synthesis, Jozef Stefan Institute, Ljubljana 1000, Slovenia

ARTICLE INFO

Keywords:
MW synthesis
IrRu electrocatalyst
OER
Water electrolysis
Durability

ABSTRACT

Under the background of renewable hydrogen generation through proton exchange membrane water electrolysis, here we report highly efficient and stable iridium (Ir) and ruthenium (Ru) alloy based electrocatalysts for the acidic OER. The electrocatalysts were synthesized by a facile microwave-assisted sodium borohydride (MW-$NaBH_4$) reduction method with 98 % reaction conversion efficiency. The ultrafine IrRu alloy nanoparticles have shown transfer of electron from Ru to Ir and *d*-band structure modification. Benefiting from the electron transfer between the active metals, the synthesized electrocatalysts have exhibited superior OER performance in acidic electrolyte. Among the combinations, the Ir-Ru (30:70) demonstrated mass activity as high as 481 A g^{-1} and requiring overpotential of 270 mV to deliver a current density of 10 mA cm^{-2}, better performance compared to other synthesized and commercial electrocatalyst. Further, Ir-Ru (50:50) have exhibited the best OER performance of 425 A g^{-1} mass activity, double to that of commercial IrO_2 and retained around 50 % of their initial current density (IrO_2 remains only 31 %) in long-term AST tests. Based on the solution electrochemical performance such as low overpotential (310 mV vs. 330 for IrO_2), high mass activity and long-term stability the Ir-Ru (50:50) alloy combination can be considered a promising electrocatalyst for PEMWE applications.

1. Introduction

Hydrogen is a fundamental energy carrier and guaranteed as one of the imperative sustainable energy sources and feedstock in modern societies. Industries and other energy sectors are dependent on blue hydrogen from natural gas generating carbon emission into the environment. Carbon emissions can be avoided, if hydrogen is produced through renewable water electrolysis [1–3] such as alkaline electrolysis [4], solid oxide electrolysis [5] and proton exchange membranes water electrolysis (PEMWE) [6–10]. Among the options, PEMWE is the most promising technology due to its advantages of flexible operating power conditions, high power density, and hydrogen purity [10] Nevertheless, PEMWE components are highly expensive and scarce, moreover the acidic operating condition of the oxygen evolution reaction (OER) at anode can threaten the future commercial implementation of this technology [11]. Modern PEMWE anodes utilizes Ir around 2 mg cm^{-2} while the Department of Energy of the United States defined a target of less than 0.125 mg cm^{-2} of Ir at anode by 2031. Ir is one of the rarest elements on earth which the European Commission has placed on its critical raw material list [12]. Ir can be extracted as a byproduct of Pt and Pd refinery, so its volume is highly dependent on Pt demand [13,14]. Further, Ir natural resources are unbalanced with major reservoirs originating from South African and Russia [15,16]. Given the state-of-the-art quantity of 2 mg cm^{-2}, the PEMWE technology at an extent of multiple GW yearly would need all the global Ir reserves [14,17]. In addition to the Ir scarcity and cost, other components such as Ti plates and PFSA membranes also contribute to the total cost of PEMWE technology.

An economic and efficient anode electrocatalyst layer is an essential objective for the commercial implementation of the PEMWE technology [14,18,19]. This can be achieved by either sustainable recycling [20,21] or lowering the Ir content with an excellent increase in the electrocatalytic activities. Generally, there are two approaches to design and develop efficient anode electrocatalysts: (*i*) electrocatalysts with higher electrochemically active surface area and (*ii*) electrocatalysts with higher specific activities. In the first method smaller Ir nanoparticles (Ir-

* Corresponding authors.
E-mail addresses: rash@igt.sdu.dk (R. Sharma), mashu@igt.sdu.dk (S.M. Andersen).

https://doi.org/10.1016/j.apsusc.2025.163405
Received 19 February 2025; Received in revised form 12 April 2025; Accepted 29 April 2025
Available online 1 May 2025

NPs) are developed carrying maximum exposed surface with respect to the mass. They are usually dispersed on conductive support which provide stable anchoring and electronic contact under operation. It has been observed that the supported electrocatalysts show better Ir-NPs dispersion, lower agglomeration and higher efficiency with maximum utilization of the active sites and reduced Ir loading [22–24]. However, identifying and implementing suitable conducting support materials is a challenge [22,24]. The second approach is the modification of the electrocatalytic active phase of the Ir that would increase the intrinsic activity. This approach is most commonly alloying Ir with other metal atoms (such as Ru, Pt, Ni, Pd) which generates structural as well as electronic modification [25–28].

Iridium and iridium oxides (Ir-IrO_x) are the most selected acidic OER electrocatalysts so far presenting the suitable activity and long-term stability [29–31]. Furthermore, ruthenium and ruthenium oxides (Ru-RuO_x) are also considered as one of the excellent acidic OER materials due to their high electrocatalytic activity. However, the long-term stability of Ru-RuO_x under acidic OER is less satisfactory. To develop a trade-off between activity and stability many methods have been explored to produce mixed element materials based on Ir and Ru components. Bimetallic Ir and Ru oxides ($Ir_xRu_{1-x}O_2$) with different compositions are generated to achieved superior OER electrocatalytic performance both activity and long-term stability in comparison to the IrO_x and RuO_x individual electrocatalysts [32,33]. It is reported in the literature that core–shell structures (Ru@IrO_x, IrRu@Ir) can prevent the oxidation and dissolution of Ru during the OER process; however, the electrocatalytic active decreases [34–36]. On the other hand, heterogeneous structures were synthesized such as IrRu@WO_3 for high OER activity and stability [37]. Kim et al. have reported trimetallic structures composed of Ir, Ru and Os ($Ir_{0.75}Ru_{0.25}Os_3$, $Ir_{0.5}Ru_{0.5}Os_3$, $Ir_{0.25}Ru_{0.75}Os_3$) in different compositions and were identified better OER electrocatalysts that their bimetallic counter parts (Ir_1Os_3, Ru_1Os_3) [38]. Qin et al. have reported 1D monoclinic Ir and Ru oxide solution (m-$Ir_{0.91}Ru_{0.09}O_{2-\delta}$) that demonstrated OER overpotential up to 180 mV at 10 mA cm^{-2} and superior long-term stability in the PEM electrolyzer setup for 256 h at 1.8 V [39]. Bertheussen et al. have synthesized IrRu supported on antimony-doped tin oxide (ATO) using solvothermal flow. The supported electrocatalysts synthesized in the presence of Ni have exhibited OER activity up to 360 mA mg_{PGM}^{-1} at 1.5 V which is 7 times higher than the activity of commercial IrO_x benchmark and two times higher than synthesized IrRu/ATO without Ni [40]. All these materials presented high OER activity due to electronic structure modification and improved active site distribution [41]. Nearly all procedures developing IrRu-based materials for OER are complicated chemical processes, time consuming chemicals reactions, convective type heating methods with low product yield or extra high temperature calcinations which is not scalable. Importantly, the electrocatalysts obtained are mostly IrRuO_x and not the elemental IrRu composition which is sometimes compromising the intrinsic active sites and the desired electronic structure modification. Thus, there is an extensive need to develop new synthesis protocols that are facile and can generate efficient and stable IrRu electrocatalysts with a strong alliance between stability and activity with high yield and conversion efficiency.

Herein, we carried batch synthesis of narrow size Ir-Ru alloy electrocatalysts for acidic OER through microwave-assisted $NaBH_4$ (MW-$NaBH_4$) reduction method. Microwave heating has the advantages of fast reaction time, product yield and quality, good particles nucleation, efficient nano-crystallization and morphology control over the convective-type heating [24,42]. The electrocatalysts were synthesized in maximum yield and in different proportions of the constitutes to investigate the effect of structure change in connection with the performance of the IrRu-based materials. The synthesized materials in different Ir and Ru proportions were screened for their OER performance in acidic solution. A trade-off between activity and stability was identified as the Ir-Ru (30:70) showed high activity while Ir-Ru (70:30) showed high long term-stability.

2. Experimental

2.1. Chemicals

Ammonium hexachloroiridate(VI) ($(NH_4)_2IrCl_6$; Sigma-Aldrich), ruthenium(III) chloride hydrate ($RuCl_3{\cdot}xH_2O$; Sigma-Aldrich), sodium borohydride ($NaBH_4$; 98 %, Sigma-Aldrich), ultrapure water (milliQ; resistivity > 18.2 MΩ cm) and perchloric acid ($HClO_4$; 70 % Suprapur®; Sigma-Aldrich) for preparing the electrolyte were used without further treatments.

2.2. Synthesis

The electrocatalysts in different proportions of Ir and Ru were synthesized by $NaBH_4$ reduction method under the microwaves (MWs) [24,43]. Representative synthesis of $Ir_{0.5}Ru_{0.5}$ was processed by dissolving $RuCl_3{\cdot}xH_2O$ in 30 mL distilled water to a concentration of 5 mmol L^{-1} in 100 mL round bottom flask. The reaction assembly, 100 mL flask connected to a cooling condenser, was fixed inside a CEM Discovery SP MW® synthesizer. Each reaction was tried for 30 mg theoretical quantity of IrRu alloy at maximum power of 200 W and at temperature of 100 °C under magnetic stirring. To trigger base Ru nuclei growth, 1.5 mL of $NaBH_4$ solution (0.75 mmol L^{-1}) was injected dropwise into the reaction flask. To the Ru base nuclei, solution of $(NH_4)_2IrCl_6$ (15.6 mL of 5 mmol L) was added into the reaction flask followed by immediate injection of the $NaBH_4$ solution (2.5 mL), Fig. 1. A camera visualized solution was suddenly changed to dark black, and precipitate had appeared showing the growth of IrRu NPs. The MW reaction was completed in 8 min and the mixture was air-cooled to room temperature to prevent particles agglomeration. The IrRu alloy NPs are collected from the mother liquid at 5000 rpm for 5 min centrifugation. The collected product was washed several times with ultrapure water and dried in an oven overnight. The same procedure was repeated for the synthesis of other electrocatalysts combinations (Table 1). The following equation was used to determine the reaction conversion efficiency in percent: $\eta_c = \frac{C_i - C_f}{C_i} \times 100$, where η_c is the reaction conversion efficiency, C_i and C_f are the initial and final concentration of the reactants (Ir and Ru) in the initial solutions and in the final supernatant. The C_i and C_f were determined using a portable X-ray fluorescence spectrometer (XRF: Thermo Scientific Niton XL3t GOLDD+). The synthesized alloyed NPs are formulated as Ir-Ru (X:Y) (X and Y are the percent weight fractions of Ir and Ru) while the reference material from Alfa Aesar is labeled as IrO_2 AA.

2.3. Characterizations

Powder X-ray diffraction (PXRD) analysis of the synthesized IrRu electrocatalysts was performed on Rigaku Miniflex 600 X-ray diffractometer. The instrument was operated at a scan of 5° min^{-1} and step size of 0.02° having Cu K_α X-ray tube (λ = 1.5418 Å).

Spherical hemisphere Specs® XPS instrument was used to perform the surface oxidation state analysis of the samples. The X-ray tube was Mg K_α (1253.6 eV) and the emitted electron from the sample entering the lens detector were recorded at 90°. All the spectra were calibrated with reference to C 1*s* 284.7 eV. CasaXPS was used to fit the data with Shirley type background and Gaussian/Lorentzian asymmetric peak envelope of 30 % Lorentzian character. Peak fittings of O 1*s*, Ir and Ru characteristics peaks were carried out according to the reported reference work [44,45]. Constrains on peak intensity were applied according to the equation $2j + 1$ (for Ir 4*f*, $j = 7/2$ and $j = 5/2$). The full width at half maximum (FWHM) was selected in the range from 0.7 to 2 eV for better resolution and transmission with 25 eV constant intensity transmission.

JEOL-JEM 2000 transmission electron microscopy (TEM) was used for particle size and distribution analysis. The TEM machine was

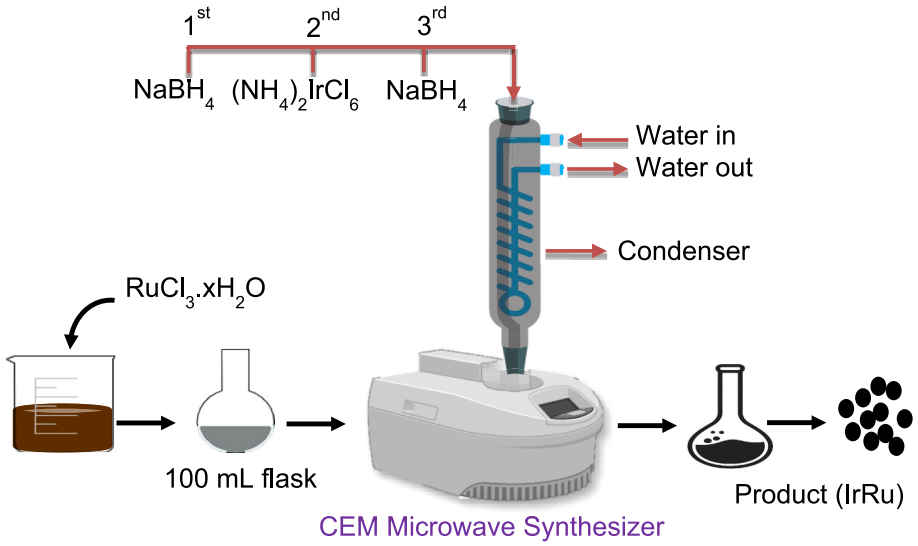

Fig. 1. Scheme showing the synthesis of IrRu-based electrocatalysts under the MW-$NaBH_4$ reduction method.

Table 1
The synthesized electrocatalysts obtained with different reaction concentrations and calculated reaction conversion efficiency.

Samples	Ir (wt.%)	Ru (wt.%)	$V_{(Ir:\ 5\ mM)}$ (mL)	$V_{(Ru:\ 5\ mM)}$ (mL)	$NaBH_4$ (mol L^{-1})	Time (min)	Conversion (%)
Ir-Ru (100:0)	100	0	31.2	–	0.75	8	98
Ir-Ru (70:30)	70	30	22.0	07.1	0.75	8	98
Ir-Ru (50:50)	50	50	15.6	30.0	0.75	8	98
Ir-Ru (30:70)	30	70	09.4	41.5	0.75	8	98
Ir-Ru (0:100)	0	100	–	59.5	0.75	8	98

equipped with thermionic source and operated at 200 kV. The TEM particle sizes of the electrocatalysts were determined from the mean diameter of 50–200 visible particles.

The XRF measurements were carried out, according to the reference procedure reported [46], to determine the metal content in the thin electrocatalyst layer deposited on glassy carbon electrode before electrochemical tests.

2.4. Electrochemical tests

The electrocatalysts ink was prepared by ultrasound dispersing 10 mg of the sample in 5 mL of the Nafion stock solution (1.84 vol% of 5 wt % Nafion-D521; IonPower, 20 vol% of 2-propanol, and 78.16 vol% of milli-Q® water). 10 μL of the ink (around 0.1 mg cm^{-2} theoretical metal content) was dropped on rotating disk glassy carbon electrode (RD-GCE: 0.196 cm^2) and was dried at 700 rpm. After drying the metal content in the electrocatalyst layer (EL) was determined using portable XRF standard procedures. The cell assembly consisted of RD-GEC|EL as the working electrode, Pt wire as the counter electrode and Ag/AgCl (sat. KCl) as the reference electrode. The reference electrode potential was converted to the reversible hydrogen electrode (RHE) potential. ZahnerIM6e workstation was used to conduct electrochemical measurements [47]. First, the working electrode was exposed to 20 cyclic voltammetry (CV) cycles in acid electrolyte (0.1 mol L^{-1} $HClO_4$ solution) from 1 to 1.7 V vs. RHE (100 mV s^{-1}) at 1600 rpm for initial activation. Then, the oxygen evolution reaction tests were conducted, and the hydrodynamic polarization curves were recorded in the potential window of 1–1.65 V vs. RHE (10 mV s^{-1}) at 1600 rpm. The potential was *iR* compensated with 2 Ω, equivalent to 70 % of the open circuit potential resistance. The experimental currents were normalized with the working electrode surface area to get the current density (J_{geo}: mA cm^{-2}). The OER onset potentials (E_{onset}) were obtained from the joining points of two tangents: one drawn from the base and other drawn from the faradic region of the curve. The overpotentials (E_{over}) were calculated at 10 mA cm^{-2}. The mass activities (J_m: A g^{-1}) were obtained by dividing the OER current with mass of the Ir-Ru content on RD-GCE. Standard accelerated stress test (AST) protocol [48] was used to monitor the long-term stability of the electrocatalysts.

3. Results and discussions

3.1. Yield of the reactions (η_c)

The concentration of the unreacted precursor content (Ir^{4+}, Ru^{3+}) after each reaction completion was systematically monitored via XRF analysis to determine the reaction conversion efficiency and yield of the MW-$NaBH_4$ reduction method. Percent conversion up to 98 % was determined for every reaction carried out (Table 1). It is worth mentioning that MW-$NaBH_4$ reduction method is more efficient than other reduction methods like polyol [22,23], high product yield with complete reduction of the precursor ions (Ir^{4+}, Ru^{3+}) to elemental nanoparticles. As reported earlier, $NaBH_4$ can lower the media pH to 1 that plays a crucial role in controlling the IrRu NPs size and distribution [24,49].

3.2. Macrostructural characterization

The structural investigation, in bulk of the synthesized electrocatalysts Ir-Ru, was performed using the powder X-ray analysis. In the PXRD pattern of Ir-Ru (100:0) (Fig. 2), clear diffraction peaks were observed at $2\theta = 40.7°$, 46.7°, 69.2°, and 83.5° corresponding to the (1 1 1), (2 0 0), (2 2 0) and (3 1 1) indices of the face centered cubic (*fcc*) metallic iridium (JCPDS: 87-0715).[50] When 30 wt% of ruthenium was added, reflections were observed corresponding to the *fcc* structure of iridium which means that Ir-Ru (70:30) have metallic phase remains in the *fcc* structure, no *hcp* structure is visible in the PXRD pattern. The

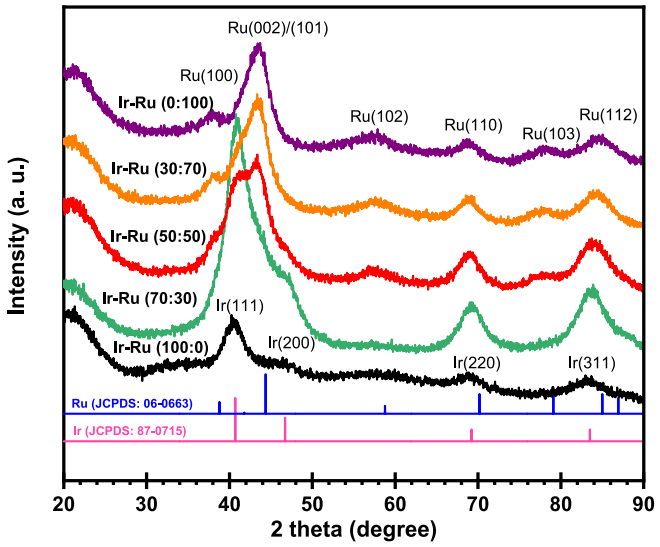

Fig. 2. PXRD patterns of the Ir-Ru alloy series electrocatalysts.

reflections of *fcc* structure shift slightly with addition of metallic Ru showing the formation of Ir-rich *fcc* alloy [51]. When the Ru amount was increased to 50 wt%, the *hcp* phase appeared along with the *fcc* phase. The coexistence of the *fcc* and *hcp* structures indicate a miscibility gap due to the different structures of pure metallic Ir *fcc* and metallic Ru *hcp* [52]. This miscibility gap was experimentally observed for the electrocatalysts having 50 wt% concentration of each metal (Ir-Ru (50:50)). Beyond the minimal composition of 50 wt%, only the metallic *hcp* reflections appeared at 2θ = 38.0°, 43.4°, 57.6°, 68.8°, 77.9° and 84.3° corresponding to the (1 0 0), (0 0 2)/(1 0 1), (1 0 2), (1 1 0), (1 0 3), and (1 1 2) miller indices of ruthenium (JCPDS: 06-0663) showing the Ru-rich *hcp* metal alloy [38,51]. Further, the Ir-Ru(0:100) electrocatalyst have peaks at 2θ = 38.0°, 43.5°, 57.7°, 68.9°, 78.4°and 84.9° corresponding to the hexagonal close pack (*hcp*) metallic ruthenium (JCPDS: 06-0663) [50]. No corresponding peaks of IrO_x and RuO_x were observed in the PXRD pattern showing that MW-$NaBH_4$ synthesis is efficient in producing metallic alloy NPs. The Scherrer equation $D_{cryst} = 0.9\lambda/\beta\cos\theta$ was used to calculate the crystallite size of the IrRu alloy nanoparticles using 2θ = 40.7° or 43.5° peak and the average D_{cryst} was around 2 nm [50].

3.3. Microstructural characterization

Selected electrocatalysts were TEM characterized to identify the particle size and distribution. The electrocatalytic performance is dependent on particle size as the mass activity increase while specific activity decrease with decrease in particle size [53]. The TEM images of the electrocatalysts Ir-Ru (50:50) and Ir-Ru (70:30) having promising OER results are presented in Fig. 3a–f. The TEM images presented in Fig. 3a–c have spherical particles aggregates are widely distributed, and the histogram was plotted from 200 spherical like units having average particle size of around 3.2 ± 0.7 nm (Fig. 4a). The TEM images presented in Fig. 3d–f have agglomerated morphology with crystalline appearance at the edges and the histogram from 80 spherical like units have average at 3.3 ± 0.74 nm (Fig. 4b). There is a slight difference in the average particle's sizes of the representative electrocatalysts, visible particles at edges in TEM images, however, the morphology of Ir-Ru (70:30) is more aggregated that can be attributed to the unequal proportion of the two elements. Representative electrocatalyst image of the selected area electron diffraction (SAED) shown in Fig. S1 have circles assigned to the lattice planes of Ir and Ru amorphous alloy (Table S1).

3.4. Surface structural characterization

The surface and electronic structure of the synthesized electrocatalysts were characterized by X-ray photoelectron spectroscopy (XPS). The presence of Ir, Ru, O and C content can be comparatively identified in Ir-Ru (70:30) and in Ir-R (50:50) from the full XPS spectra (Fig. S2). From the smooth background CasaXPS function, the surface atom content for Ir is 8.2 % and for Ru is 4.1 % in Ir-Ru (70:30) while the atom content for Ir is 4.3 % and for Ru is 4.4 % in Ir-Ru (50:50) (Table S2) which is much close to the theoretical ratio of the two metals content.

It is reported in the literature that the electronic state of the active metal is highly important for enhanced OER performance [23]. The electronic state and relative amount of each electronic component of Ir, Ru and O in Ir-Ru (70:30) and in Ir-R (50:50) representative high OER performing electrocatalysts are identified using high resolution and best statistics XPS spectra. Fig. 5a show the spin–orbit doublet of Ir $4f_{7/2}$ and Ir $4f_{5/2}$. Each component is divided into two deconvoluted peaks with prominent areas fitted at 61.0 and 63.2 eV [Ir-$_{0.7}$Ru (70:30)] and at 60.8 and 62.4 eV [Ir-Ru (50:50)] corresponding to the Ir^0 and Ir^{4+} (Table 2) [44], respectively. The core XPS spectra of Ru 3*p* (Fig. 5b) has doublets of Ru $3p_{3/2}$ and Ru $3p_{1/2}$ where the prominent fitting is located at 462.2 and 465.2 eV for Ir-Ru (70:30) and at 461.6 and 463.2 eV for Ir-Ru

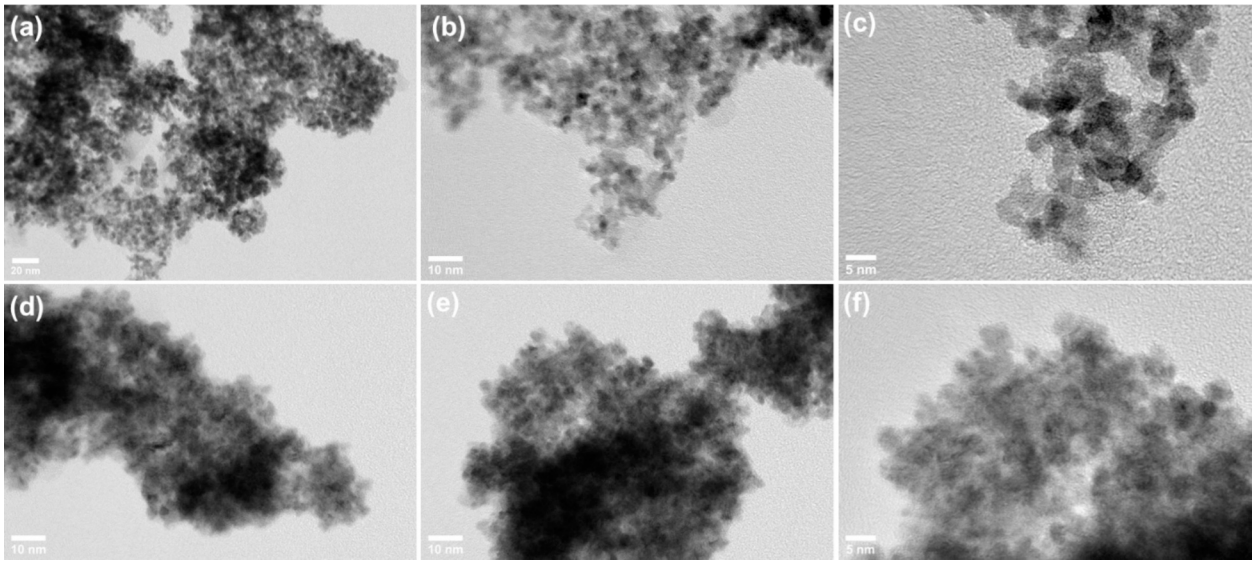

Fig. 3. TEM images of Ir-Ru (50:50) (a–c) and Ir-Ru (70:30) (d–f).

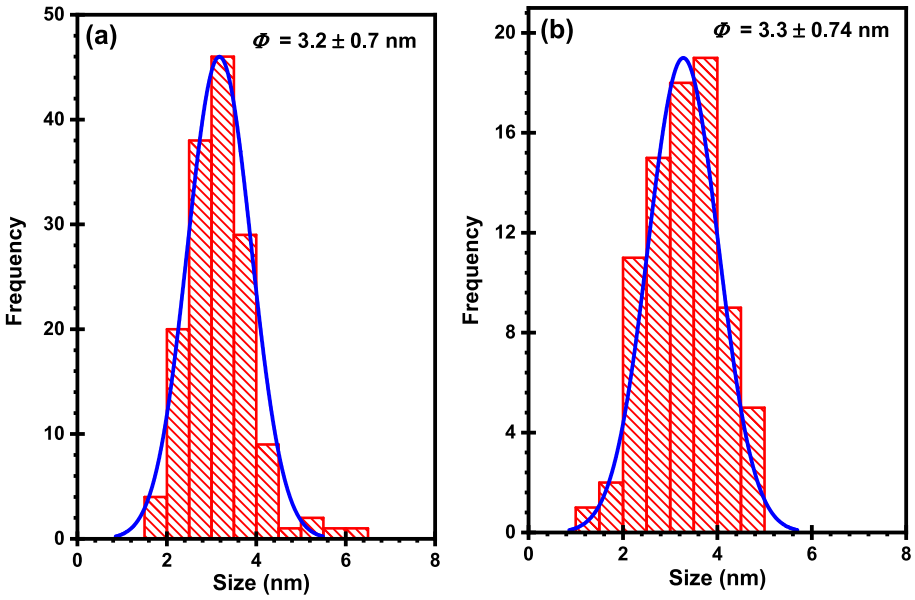

Fig. 4. TEM particles size histograms obtained by measuring visible 200 spherical and hemispherical particles of Ir-Ru (50:50) (a) and by measuring visible 80 spherical and hemispherical particles of Ir-Ru (70:30) (b).

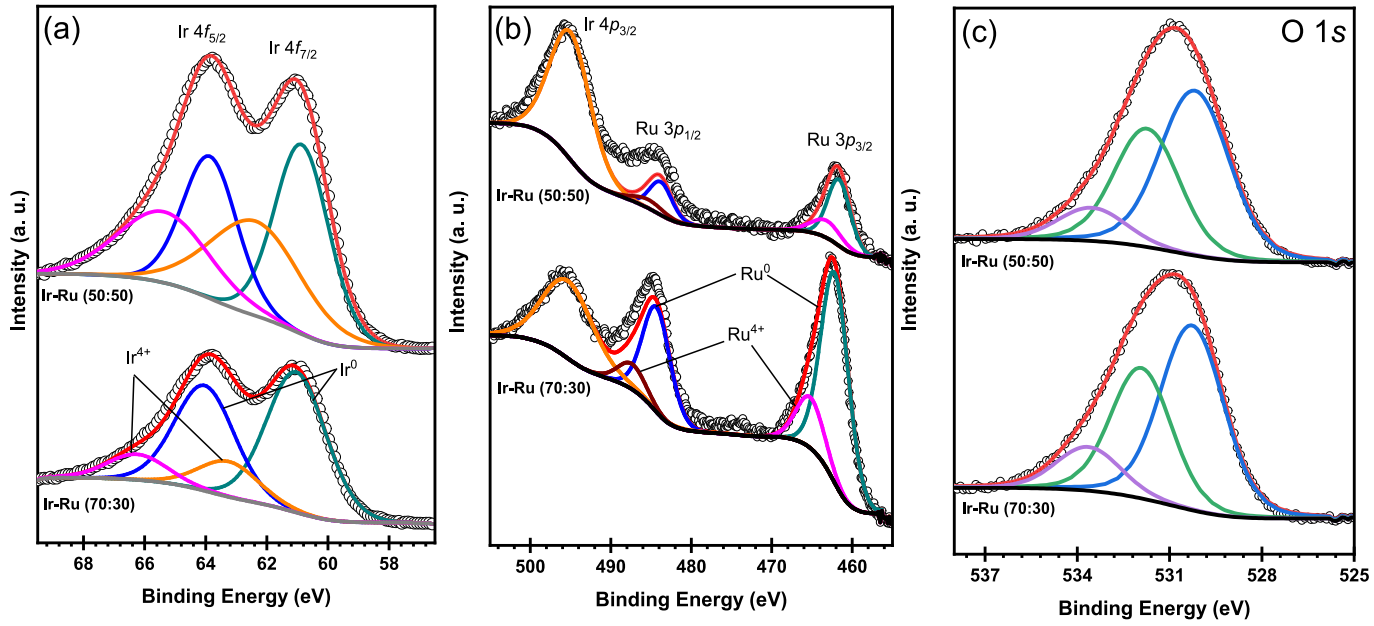

Fig. 5. High resolution XPS spectra of Ir 4*f* (a), Ru 3*p* (b), and O 1*s* (c) in Ir-Ru (70:30) and Ir-Ru (50:50) electrocatalysts, respectively.

(50:50) corresponding to the Ru^0 and Ru^{4+} (Table 2), respectively. The Ir 4*d* also have two doublets with peaks at 296.3 eV and 298.7 eV for Ir-Ru (70:30) and at 295.8 eV and 298.0 eV for Ir-R (50:50) corresponding to the Ir^0 and Ir^{4+} along with satellite peaks at 304.2 eV (Fig. S3a and Table 2). Fig. S3b shows the spin–orbit doublet for Ru $3d_{5/2}$ and Ru $3d_{3/2}$. Each peak was fit into two sub-peaks corresponding to Ru^0 at 280.1/284.3 eV and to Ru^{4+} at 281.4/285.6 eV in Ir-Ru (70:30) and to Ru^0 at 279.9/284.1 eV and to Ru^{4+} at 281.2/285.4 eV in Ir-R (50:50) (Table 2) [45]. Peak at 284.5 eV was assigned to C 1*s*. The peak area of Ir^0 $4f_{7/2}$ is 45.6 % and of Ir^{4+} $4f_{7/2}$ is 11.3 % while the peak area of Ru^0 $3d_{5/2}$ is 28.5 % and of Ru^{4+} is 8.7 %, showing that elemental Ir and Ru are dominant in Ir-Ru (70:30). It can be seen in the high resolution XPS data of Ir 4*f* peaks in both Ir-Ru (70:30) and Ir-Ru (50:50) *versus* reference Ir value (61.4 eV) [24] are shifted to lower binding energy by 0.6 eV, indicating the more reduced valance state of Ir in the selected electrocatalysts. On the other hand, the Ru 3*p* peaks in both Ir-Ru (70:30) and Ir-Ru (50:50) versus reference Ru value (461.2 eV) [45] are shifted to higher binding energy. The ionization enthalpy of Ru (710.2 kJ mol^{-1}) is lower than Ir (865.2 kJ mol^{-1}) facilitating the transfer of electron from Ru to Ir that may cause *d*-band structure modification and high electrochemical stability [39]. The O 1*s* can be fitted into three peaks at 530.3, 531.9, and 533.6 eV for $Ir_{0.7}Ru_{0.3}$ and at 530.2, 531.7, and 533.5 eV for Ir-R (50:50) corresponding to metal-O, defected-O, and vacancy-O (Fig. 5c and Table 2), respectively [39]. The XPS results clearly show that the alloy composition is predominantly metallic, however traces of Ir-Ru-O_x, with roughly estimated 20 % oxygen, may also be present both on the surface and in the surface bulk.

Table 2
High resolution XPS binding energies and the percent atomic amount of each component of the representative electrocatalysts.

Electrocatalysts→	Ir-Ru (70:30) [This work]		Ir-Ru (50:50) [This work]		Ref. [Ir [24], Ru [45],O [39]]
Peaks↓	BE (eV)	Area (%)	BE (eV)	Area (%)	BE (eV)
Ir^0 $4f_{7/2}$	61	45.6	60.8	31.2	61.4
Ir^0 $4f_{5/2}$	64	34.5	63.8	23.4	
Ir^{4+} $4f_{7/2}$	63.2	11.3	62.4	25.9	63.4
Ir^{4+} $4f_{5/2}$	66.2	8.6	65.4	19.4	
Ru^0 $3p_{3/2}$	462.2	39.4	461.6	18.5	461.2
Ru^0 $3p_{1/2}$	484.3	19.5	483.8	19.1	
Ru^{4+} $3p_{3/2}$	465.2	9.5	463.2	6.4	462.6
Ru^{4+} $3p_{1/2}$	487.4	4.7	485.3	3.2	
Ir^0 $4p_{3/2}$	495.3	26.8	495	62.7	
Ir^0 $4d_{5/2}$	296.3	38.3	295.8	30.7	296.2
Ir^0 $4d_{3/2}$	311.5	24.7	311.6	20.4	
Ir^{4+} $4d_{5/2}$	298.7	9.7	298	17.4	298.6
Ir^{4+} $4d_{3/2}$	313.9	6.3	313.8	11.6	
Ir 4*d*-sat.	304.2	21	304.2	19.9	
Ru^0 $3d_{5/2}$	280.1	28.5	279.9	24.5	279.9
Ru^0 $3d_{3/2}$	284.3	18.5	284.1	16.4	
Ru^{4+} $3d_{5/2}$	281.4	8.7	281.2	13.6	280.7
Ru^{4+} $3d_{3/2}$	285.6	5.7	285.4	9.1	
C 1*s*	284.5	38.6	284.8	36.4	
O1 (O 1*s*)	530.3	52.3	530.2	53.5	metal-O
O2 (O 1*s*)	531.9	35.2	531.7	36.1	defect-O
O2 (O 1*s*)	533.6	12.5	533.5	10.4	vacancy-O

3.5. Electrochemical activity measurements

The OER polarization curves of the synthesized Ir-Ru alloy electrocatalysts were recorded using cyclic voltammetry (CV) and the results were compared to that of commercial material under similar conditions. The two-tangent joining point onset potential (E_{onset}) of the synthesized electrocatalysts is lower than the onset potential (E_{onset}) of the commercial IrO_2 (E_{onset}: 1.49 for IrO_2) Fig. 6a and Table 3, confirming that the alloy electrocatalysts are much active toward OER. Most of the synthesized electrocatalysts exhibited low overpotential (E_{over}, calculated at 10 mA cm^{-2}) than that of commercial materials. Electrocatalysts such as Ir-Ru (50:50), Ir-Ru (30:70), and Ir-Ru (0:100) have E_{over} equal to 310 mV, 270 mV and 310 mV (Fig. 6b and Table 3), respectively which is much lower than the E_{over} of IrO_2 (330 mV). Rating the electrocatalysts based on the E_{over} value, the Ir-Ru (30:70) alloy composition is the most efficient electrocatalyst with minimum over-potential (60 mV lower than IrO_2) to generate 10 mA cm^{-2} OER current under acidic conditions. This can be attributed to the elemental alloy composition in appropriate quantity of ruthenium major portion and uniform particle size of around 2 nm. There are numerous articles reporting the Ir and Ru compositions like Ir-Ru oxide solution prepared in 1D monoclinic forms with varying active metal contents. The electrocatalysts have presented overpotential up to 180 mV for m-$Ir_{0.9}Ru_{0.09}O_{2-\delta}$, 255 mV for m-$Ir_{0.65}Ru_{0.35}O_2$, 259 mV for m-$Ir_{0.87}Ru_{0.13}O_2$, 271 mV for m-$Ir_{0.94}Ru_{0.06}O_2$, and 286 mV for m-$Ir_1Ru_0O_2$ at 10 mA cm^{-2} [39]. Nanowires (NWs) of IrRu alloy and pure Ir have shown overpotential of 243 mV and 290 mV, respectively, at 10 mA cm^{-2} [54]. Ultrafine IrRu intermetallic nanoclusters supported on conductive and amorphous tellurium nanoparticles were hydrothermally synthesized. The electrocatalysts (IrRu@Te) have demonstrated mass activity of 590 A g^{-1} with an overpotential of 270 mV [55]. Low overpotential up to 191 mV for acidic OER has been presented by vertically stacked amorphous Ir/Ru/Ir

Table 3
Electrochemical relative performance data of the Ir-Ru alloy and commercial IrO_2.

Electrocatalysts	$i_{initial}$@1.65 V (mA)	E_{onset} (V)	E_{over} (mV)	J_{geo} (mA cm^{-2})	$J_{mIr\text{-}Ru}$ (A g^{-1})
Ir-Ru (100:0)	4.50	1.47	330	3.75	260
Ir-Ru (70:30)	3.14	1.51	370	1.17	149
Ir-Ru (50:50)	5.02	1.44	310	5.89	425
Ir-Ru (30:70)	6.25	1.41	270	10.3	481
Ir-Ru (0:100)	4.84	1.44	310	6.13	281
IrO_2 AA	5.28	1.49	330	3.31	305

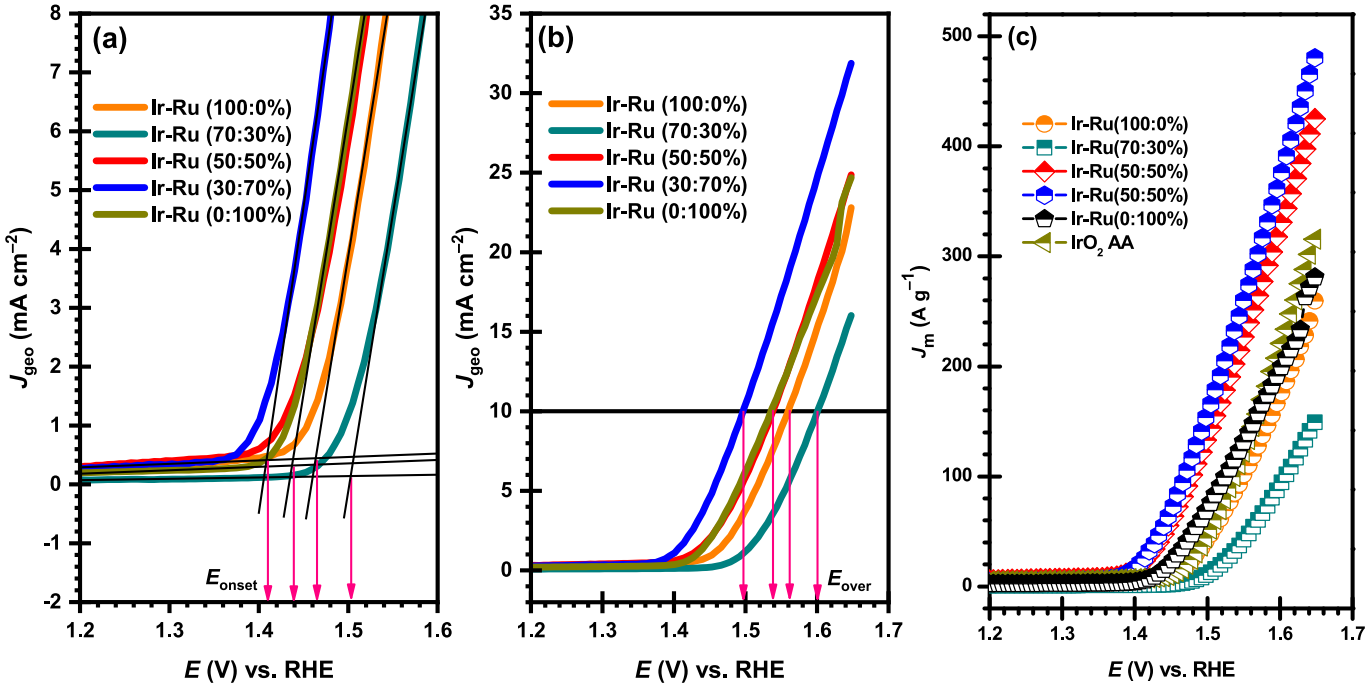

Fig. 6. Specific activities showing the onset potential (a) and the overpotential (b) of the Ir-Ru electrocatalysts. Mass activates (c) of the Ir-Ru electrocatalysts.

oxides nanosheets developed through segregation approach [56]. Most of the Ir-Ru alloy electrocatalysts have presented better specific activities (J_{geo}) than commercial IrO_2 at 1.5 V vs. RHE, Fig. 6b and Table 3. The decreasing order of their specific activities is Ir-Ru (30:70) > Ir_0Ru (0:100) ≈ Ir-Ru (50:50) > Ir-Ru (100:0) > Ir-Ru (70:30). This shows a relationship between the relative amount of Ru and specific activity that the activity declines with decreasing amount of ruthenium (y < 50 wt% for Ru and x > 50 wt% for Ir). More specifically, low OER activity has been presented by iridium dominating electrocatalyst Ir-Ru (70:30) while better OER activity has been presented by Ir-Ru (50:50). However, there is a negligible difference between the average particle sizes of Ir-Ru (50:50) (3.2 nm) and Ir-Ru (70:30) (3.3 nm). This is how our postulate of trade-off between activity and stability develops where Ru is promoting the activity while Ir is promoting stability. The highly specific activity of the Ir-Ru alloy *versus* the reference commercial IrO_2 is due to the MW-$NaBH_4$ synthesis method where elemental alloy NPs in appropriate combination and in good yield were generated with uniform particles size. The electrocatalysts total mass normalized OER polarization curves are given in Fig. 6c while mass activities data at 1.65 V vs. RHE is given in Table 3. Among the Ir-Ru alloy compositions, high mass activities were obtained for Ir-Ru (30:70) alloy (J_m = 481 A g^{-1}) and for Ir-Ru (50:50) alloy (J_m = 425 A g^{-1}) than for the other synthetic combinations where Ru is a dominating element and for the commercial IrO_2. The same electrocatalysts have also presented the highest initial current ($i_{initial}$: 6.25 mA and 5.02 mA) at 1.65 V vs. RHE than other electrocatalysts. Total mass activities up 260 A g^{-1} and 281 A g^{-1} is also recorded for Ir-Ru (100:0) and Ir-Ru (0:100) which are low mass activities than commercial IrO_2. The high mass activities of Ir-Ru (30:70) and Ir-Ru (50:50) can be attributed to the alloyed NPs developed under MW-$NaBH_4$ reduction method with appropriate metallic combination with uniform narrow particles size.

3.6. Electrokinetic measurements

Water splitting proceeds through series of four electron paired proton transfer reactions over the same surface-active metal site (**M**−), Eqs. (1)–(4) [54,57]. During these reaction reactions reactive intermediates such as —OH and —OOH are generating along with pair of electron and proton. Based on the mechanism and applied potential versus current relationship, the Tafel slope of the OER can be derived as 2.303 *RT*/(0.5*n*), where *R* gas constant, *T* is absolute temperature and *n* is the number of electron transfers defining the rate determining step. For every rate determining step the Tafel slope is different [54]. For example, if the rate determining step is Eq. (1), the Tafel slope is 120 mV dec^{-1} and if the rate determining step is Eq. (2) then the Tafel slope is 40 mV dec^{-1} [54]. As most of the Ir-Ru alloy combinations of the current studies have shown Tafel slope lower than 120 mV dec^{-1} so the rate determining step is Eq. (2). Among the synthesized electrocatalysts, the Ir-Ru alloy with 30:70 % composition have shown the low Tafel slop showing the fast OER kinetics, Fig. 7. Nevertheless, comparable kinetics have also been observed for the other combinations such as Ir-Ru (70:30) with slope of 73 mV dec^{-1} and Ir-Ru (0:100) with slope of 74 mV dec^{-1} show good OER kinetics although the overall activities of these electrocatalysts are lower than Ir-Ru (30:70).

$$\mathbf{M}-H_2O \rightarrow \mathbf{M}-OH + e^- + H^+ \quad (1)$$

$$\mathbf{M}-OH \rightarrow \mathbf{M}-O + e^- + H^+ \quad (2)$$

$$\mathbf{M}-OH + H_2O \rightarrow \mathbf{M}-OOH + e^- + H^+ \quad (3)$$

$$\mathbf{M}-OOH \rightarrow O_2(g) + \mathbf{M} + e^- + H^+ \quad (4)$$

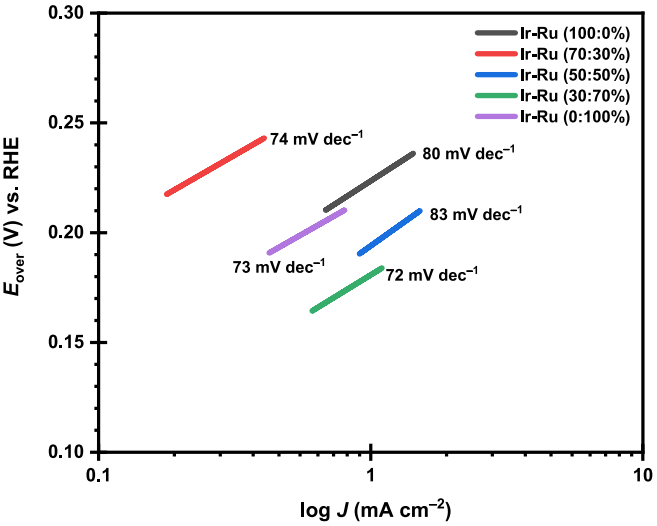

Fig. 7. Tafel slopes of the synthesized Ir-Ru alloys.

3.7. Electrochemical stability measurements

The electrochemical stability of the synthesized Ir-Ru alloy electrocatalysts studies using standard accelerated stress (AST) procedures. The AST implicates stepwise revelation of the working electrode to potential stress and is safer from chronopotentiometry tests causing electrode surface corrosions [58]. The procedure is designed to apply 2000 CV cycles (1.0–1.7 V vs. RHE) at 100 mV s^{-1} to the working electrode (RDE|GCE|EL) which are disrupted by 2 observational CV cycles between 1.0 and 1.65 V vs. RHE at 10 mV s^{-1} (after specific number of stress cycles) [48]. The retained current density in percent of each step is calculated from the initial and final OER currents at 1.65 V vs. RHE. The AST performance of the synthesized electrocatalyst is shown in Fig. 8 and the data is tabulated in Table S3. The electrocatalyst having the highest stability among the options is Ir-Ru (100:0) with no ruthenium content that retains about 60 % of their initial current density. In the alloyed compositions, the Ir-Ru (70:30) retain about 50 % while Ir-Ru (50:50) retain about 45 % of their initial current densities which are higher than commercial IrO_2 with a retained current density of 31 %. However, the specific activity of Ir-Ru (70:30) was 1.17 mA cm^{-2} at 1.5 V, lowest among the options. Minimum electrochemical stability has been presented by Ir-Ru (30:70) and Ir-Ru (0:100) compositions with below 5 % of their initial current densities retained. However, the specific activity of Ir-Ru (30:70) was 10.3 mA cm^{-2} at 1.5 V, highest among the options. The lower acidic OER AST stability of the Ru dominating electrocatalysts can be explained in the following two points; (*i*) the overoxidation of Ru to soluble RuO_4 under acidic OER, and (*ii*) the surface demetallation resulted in aggregates and structural failure [59]. A feasible way to maintain the stability of the Ru-based electrocatalysts is to stabilize the lattice oxygen and surface of Ru in acidic media. Herein, we were able to significantly improve stability by combining Ir and Ru in different proportions and $Ir_{0.7}Ru_{0.3}$ and $Ir_{0.5}Ru_{0.5}$ were evidently identified superior OER stable electrocatalysts. The high AST stability of Ir-Ru (70:30) and Ir-Ru (50:50) can be attributed to the alloyed NPs having the appropriate amount of Ru incorporated that stabilized the lattice oxygen and minimum Ru oxidation. The AST results clearly show that the electrochemical stability decreases with an increasing amount of Ru while the activity increases. Among the synthesized electrocatalyst, an excellent trade between activity and stability has been maintained by Ir-Ru (50:50) having OER activity of about 6 mA cm^{-2} (appx. 650 A g^{-1}) with 50 % retention of their initial current density. For further confirmation, post-AST TEM analysis of the Ir-Ru (50:50) was carried out to check the NPs aggregation upon exposure to the repeated potential stress. The post-AST TEM images of Ir-Ru (50:50) show that the NPs are

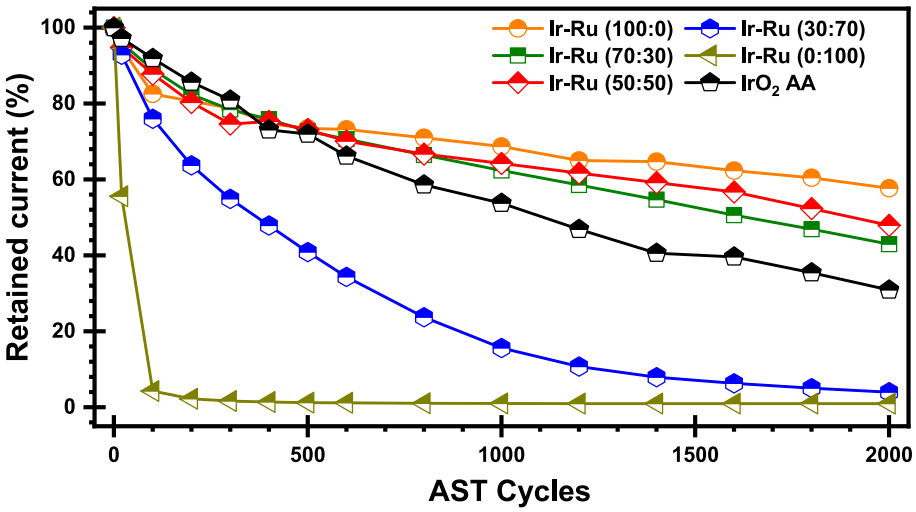

Fig. 8. Mass normalized OER polarization curves of the IrRu electrocatalysts.

still widely distributed but grown to aggregates probably due to the surface oxidation (Fig. S4). The surface oxidation of iridium can stabilize the lattice oxygen and surface Ru preventing volatile RuO_2 formation under acidic OER [54]. This simultaneous lattice oxygen stabilization and surface Ru can boost the electrocatalyst stability toward acidic OER. The post-AST histogram average particles size of $Ir_{0.5}Ru_{0.5}$ is around 3.8 ± 0.82 nm (Fig. S5). The post-AST particles grew by only 19 % to the pre-AST particle size of $Ir_{0.5}Ru_{0.5}$ showing excellent electrochemical long-term stability.

We conclude that the OER activity needs highly stable atoms surfaces with limited nanoscale separation of the particles. A good balance between activity and stability can be achieved by designing materials showing slow limited surface segregation of the nanoparticles under prolong OER operation, regenerating fresh OER active surfaces. Based on the best trade-off between activity and stability, $Ir_{0.5}Ru_{0.5}$ combination has been identified as an excellent material showed optimum activity and stability because of the limited surface segregation and structural collapse.

4. Conclusions

In summary, Ir and Ru based alloys in different weight fractions ratios (Ir:Ru = 100:0, 70:30, 50:50, 30:70, and 0:100) were synthesized using MW-$NaBH_4$ reduction method. After structural characterization, the fine NPs of IrRu were screened for their acidic OER performance. The electrocatalysts activity increased with increasing weight fraction of Ru in the alloy while stability decreased. A tradeoff between stability and activity was established proportionally with the relative amount of Ir and Ru where Ir promotes stability. Among the combinations, the Ir-Ru (30:70) (*hcp* phase) demonstrated mass activity as high as 481 A g^{-1} and requiring overpotential of 270 mV to deliver 10 mA cm^{-2} current but lower stability of only less than 5 % retained current. On the other hand, Ir-Ru (70:30) (*fcc* phase) demonstrated mass activity as low as 149 A g^{-1} and requiring overpotential of 370 mV to deliver 10 mA cm^{-2} current but high stability of around 45 % retained current. Furthermore, the Ir-Ru (50:50) (miscibility gap between *fcc* and *hcp*) also have OER mass activity up to 425 A g^{-1} and retained current of around 50 % which is the best combination among the synthesized electrocatalysts and can be consider future electrocatalyst for practical PEMWEs.

CRediT authorship contribution statement

Inayat Ali Khan: Writing – original draft, Visualization, Validation, Formal analysis, Data curation. **Per Morgen:** Writing – review & editing, Methodology, Data curation. **Saso Gyergyek:** Writing – review & editing, Formal analysis, Data curation. **Raghunandan Sharma:** Writing – review & editing, Supervision, Methodology, Formal analysis, Data curation, Conceptualization. **Shuang Ma Andersen:** Writing – review & editing, Supervision, Resources, Project administration, Methodology, Funding acquisition, Conceptualization.

Declaration of competing interest

The authors declare that they have no known competing financial interests or personal relationships that could have appeared to influence the work reported in this paper.

Acknowledgments

The Europe Union is gratefully acknowledged for financial support in the form of a stipend for I.A.K. under the MSCA grant (project number: 101150584). The authors also acknowledge financial support from Innovation Fund Denmark, InnoExplorer program, Nr. 9122-00112; Danish Agency for Higher Education and Science, ESS lighthouse on hard materials in 3D, SOLID, Grant number 8144-00002B; Energi Fyns udviklingsfond and Slovenian Research Agency (research core funding Nos. P2-0089). The authors thank the Centre of Excellence in Nanoscience and Nanotechnology–Nanocenter for the use of Transmission Electron Microscope Jeol JEM-2100.

Appendix A. Supplementary material

The supporting information is available and contains SAED pattern and data, XPS survey spectra, fitted spectra and data, AST data and post-AST TEM images and histogram. Supplementary material to this article can be found online at https://doi.org/10.1016/j.apsusc.2025.163405.

Data availability

Data will be made available on request.

References

[1] F. Barbir, PEM electrolysis for production of hydrogen from renewable energy sources, Sol. Energy 78 (2005) 661–669.
[2] M.A. Pellow, C.J. Emmott, C.J. Barnhart, S.M. Benson, Hydrogen or batteries for grid storage? A net energy analysis, Energy Environ. Sci. 8 (2015) 1938–1952.
[3] K.E. Ayers, C. Capuano, E.B. Anderson, Recent advances in cell cost and efficiency for PEM-based water electrolysis, ECS Trans. 41 (2012) 15.

[4] H. Tüysüz, Alkaline water electrolysis for green hydrogen production, Acc. Chem. Res. 57 (2024) 558–567.
[5] A. Hauch, R. Küngas, P. Blennow, A.B. Hansen, J.B. Hansen, B.V. Mathiesen, M. B. Mogensen, Recent advances in solid oxide cell technology for electrolysis, Science 370 (2020) eaba6118.
[6] J.K. Lee, G. Anderson, A.W. Tricker, F. Babbe, A. Madan, D.A. Cullen, J.D. Arregui-Mena, N. Danilovic, R. Mukundan, A.Z. Weber, Ionomer-free and recyclable porous-transport electrode for high-performing proton-exchange-membrane water electrolysis, Nat. Commun. 14 (2023) 4592.
[7] R.-T. Liu, Z.-L. Xu, F.-M. Li, F.-Y. Chen, J.-Y. Yu, Y. Yan, Y. Chen, B.Y. Xia, Recent advances in proton exchange membrane water electrolysis, Chem. Soc. Rev. 25 (2023) 5652–5683.
[8] Y. Chen, C. Liu, J. Xu, C. Xia, P. Wang, B.Y. Xia, Y. Yan, X. Wang, Key components and design strategy for a proton exchange membrane water electrolyzer, Small Struct. 4 (2023) 2200130.
[9] L. Deng, H. Chen, S.-F. Hung, Y. Zhang, H. Yu, H.-Y. Chen, L. Li, S. Peng, Lewis acid-mediated interfacial water supply for sustainable proton exchange membrane water electrolysis, J. Am. Chem. Soc. 146 (2024) 35438–35448.
[10] M. Carmo, D.L. Fritz, J. Mergel, D. Stolten, A comprehensive review on PEM water electrolysis, Int. J Hydrogen Energy 38 (2013) 4901–4934.
[11] L. Li, P. Wang, Q. Shao, X. Huang, Recent progress in advanced electrocatalyst design for acidic oxygen evolution reaction, Adv. Mater. 33 (2021) 2004243.
[12] E. Commission, Study on the Critical Raw Materials for the EU2023, 2023.
[13] P.C. Vesborg, T.F. Jaramillo, Addressing the terawatt challenge: scalability in the supply of chemical elements for renewable energy, RSC Adv. 2 (2012) 7933–7947.
[14] C. Minke, M. Suermann, B. Bensmann, R. Hanke-Rauschenbach, Is iridium demand a potential bottleneck in the realization of large-scale PEM water electrolysis? Int. J. Hydrogen Energy 46 (2021) 23581–23590.
[15] H.U. Sverdrup, K.V. Ragnarsdottir, A system dynamics model for platinum group metal supply, market price, depletion of extractable amounts, ore grade, recycling and stocks-in-use, Resour. Conserv. Recycl. 114 (2016) 130–152.
[16] K.D. Rasmussen, H. Wenzel, C. Bangs, E. Petavratzi, G. Liu, Platinum demand and potential bottlenecks in the global green transition: a dynamic material flow analysis, Environ. Sci. Technol. 53 (2019) 11541–11551.
[17] M. Bernt, A. Siebel, H.A. Gasteiger, Analysis of voltage losses in PEM water electrolyzers with low platinum group metal loadings, J. Electrochem. Soc. 165 (2018) F305–F314.
[18] U. Babic, M. Suermann, F.N. Büchi, L. Gubler, T.J. Schmidt, Critical review—identifying critical gaps for polymer electrolyte water electrolysis development, J. Electrochem. Soc. 164 (2017) F387.
[19] M. Bernt, A. Hartig-Weiß, M.F. Tovini, H.A. El-Sayed, C. Schramm, J. Schröter, C. Gebauer, H.A. Gasteiger, Current challenges in catalyst development for PEM water electrolyzers, Chem. Ing. Tech. 92 (2020) 31–39.
[20] R. Sharma, P. Morgen, S. Ma Andersen, Dissolution of nanoparticulate IrO_2 in dilute acidic baths through a pre-reduction step: a method to recover Ir from electrocatalytic/catalytic bodies, Appl. Surf. Sci. 681 (2025) 161553.
[21] R. Sharma, P. Morgen, D. Makovec, S. Gyergyek, S.M. Andersen, Enhanced electrochemical dissolution of iridium oxide in acidic electrolytes through presence of metal ions: shortened lifetime and hope for recovery, RSC Sustainability 2 (2024) 2225–2238.
[22] I.A. Khan, P. Morgen, S. Gyergyek, R. Sharma, S.M. Andersen, Selection on antimony-doped tin oxide (ATO) as an efficient support for iridium-based oxygen evolution reaction (OER) catalyst in acidic media, Mater. Chem. Phys. 308 (2023) 128192.
[23] I. Ali Khan, P. Morgen, S. Gyergyek, R. Sharma, S. Ma Andersen, Reduced valence state of iridium supported on antimony doped tin oxide as a highly active and robust oxygen evolution reaction electrocatalyst for proton exchange membrane-based electrolysis, Appl. Surf. Sci. 646 (2024) 158924.
[24] I.A. Khan, P. Morgen, R. Sharma, S.M. Andersen, Tuning on highly dispersed iridium on antimony-doped tin oxide with strong metal–support interaction for oxygen evolution reaction, ACS Appl. Energy Mater. 07 (2024) 11977–11987.
[25] A. Ruban, B. Hammer, P. Stoltze, H.L. Skriver, J.K. Nørskov, Surface electronic structure and reactivity of transition and noble metals, J. Mol. Catal. A Chem. 115 (1997) 421–429.
[26] U.B. Demirci, Theoretical means for searching bimetallic alloys as anode electrocatalysts for direct liquid-feed fuel cells, J. Power Sources 173 (2007) 11–18.
[27] X. Zhang, Y. Chen, Z. Ye, H. Hu, L. Lei, F. You, J. Yao, H. Yang, X. Jiang, Magnetic field-assisted microbial corrosion construction iron sulfides incorporated nickel-iron hydroxide towards efficient oxygen evolution, Chin. J. Struct. Chem. 43 (2024) 100200.
[28] L. Tang, Y. Wan, Y. Lin, Lowering the kinetic barrier via enhancing electrophilicity of surface oxygen to boost acidic oxygen evolution reaction, Chin. J. Struct. Chem. 43 (2024) 100345.
[29] C. Spöri, P. Briois, H.N. Nong, T. Reier, A. Billard, S. Kühl, D. Teschner, P. Strasser, Experimental activity descriptors for iridium-based catalysts for the electrochemical oxygen evolution reaction (OER), ACS Catal. 9 (2019) 6653–6663.
[30] J. Cheng, J. Yang, S. Kitano, G. Juhasz, M. Higashi, M. Sadakiyo, K. Kato, S. Yoshioka, T. Sugiyama, M. Yamauchi, Impact of Ir-valence control and surface nanostructure on oxygen evolution reaction over a highly efficient Ir–TiO2 nanorod catalyst, ACS Catal. 9 (2019) 6974–6986.
[31] C. Spöri, J.T.H. Kwan, A. Bonakdarpour, D.P. Wilkinson, P. Strasser, The stability challenges of oxygen evolving catalysts: towards a common fundamental understanding and mitigation of catalyst degradation, Angew. Chem. Int. Ed. 56 (2017) 5994–6021.
[32] J. Cheng, H. Zhang, G. Chen, Y. Zhang, Study of IrxRu1− xO2 oxides as anodic electrocatalysts for solid polymer electrolyte water electrolysis, Electrochim. Acta 54 (2009) 6250–6256.
[33] N. Danilovic, R. Subbaraman, K.C. Chang, S.H. Chang, Y. Kang, J. Snyder, A. P. Paulikas, D. Strmcnik, Y.T. Kim, D. Myers, Using surface segregation to design stable Ru-Ir oxides for the oxygen evolution reaction in acidic environments, Angew. Chem. Int. Ed. 53 (2014) 14016–14021.
[34] J. Zhang, X. Fu, F. Xia, W. Zhang, D. Ma, Y. Zhou, H. Peng, J. Wu, X. Gong, D. Wang, Core-shell nanostructured Ru@ Ir–O electrocatalysts for superb oxygen evolution in acid, Small 18 (2022) 2108031.
[35] J. Shan, C. Guo, Y. Zhu, S. Chen, L. Song, M. Jaroniec, Y. Zheng, S.-Z. Qiao, Charge-redistribution-enhanced nanocrystalline Ru@ IrOx electrocatalysts for oxygen evolution in acidic media, Chem 5 (2019) 445–459.
[36] Y. Zheng, F. Zhang, G. Wang, D. Lai, L. Zou, Q. Cheng, J. Li, Z. Zou, H. Yang, CO induced phase-segregation to construct robust and efficient IrRux@ Ir core-shell electrocatalyst towards acidic oxygen evolution, J. Power Sources 528 (2022) 231189.
[37] G. Jiang, H. Yu, D. Yao, Y. Li, J. Chi, H. Zhang, Z. Shao, Boosting the oxygen evolution stability and activity of a heterogeneous IrRu bimetallic coating on a WO 3 nano-array electrode for PEM water electrolysis, J. Mater. Chem. A 10 (2022) 11893–11903.
[38] K.-S. Kim, S.-A. Park, S.-M. Jung, J. Kwak, J.-S. Kwon, Y. Kim, H.-W. Jung, Y.-T. Kim, Deteriorated balance between activity and stability via Ru incorporation into Ir-based oxygen evolution nanostructures, ACS Catal. 13 (2023) 11314–11322.
[39] K. Qin, H. Yu, W. Zhu, Y. Zhou, Z. Guo, Q. Shao, Y. Wu, X. Wang, Y. Li, Y. Ji, 1D Monoclinic IrxRu1-xO2 solid solution with ru-enhanced electrocatalytic activity for acidic oxygen evolution reaction, Adv. Funct. Mater. (2024) 2402226.
[40] E. Bertheussen, S. Pitscheider, S.R. Cooper, R. Pittkowski, K.L. Svane, A. Bornet, E. M. Wisaeus, K.M.Ø. Jensen, J. Rossmeisl, M. Arenz, C. Kallesøe, C.M. Pedersen, Impact of nickel on iridium–ruthenium structure and activity for the oxygen evolution reaction under acidic conditions, ACS Mater. Au 4 (2024) 512–522.
[41] O. Kasian, S. Geiger, P. Stock, G. Polymeros, B. Breitbach, A. Savan, A. Ludwig, S. Cherevko, K.J. Mayrhofer, On the origin of the improved ruthenium stability in RuO2–IrO2 mixed oxides, J. Electrochem. Soc. 163 (2016) F3099.
[42] G.A. Tompsett, W.C. Conner, K.S. Yngvesson, Microwave synthesis of nanoporous materials, ChemPhysChem 7 (2006) 296–319.
[43] S.S. Karade, R. Sharma, P. Morgen, D. Makovec, S. Gyergyek, S.M. Andersen, Tailoring iridium–palladium nanoparticles with Ir-rich skin: a highly durable anode electrocatalyst for acidic water electrolysis via a facile microwave-assisted chemical reduction method, Phys. Chem. Chem. Phys. 26 (2024) 9060–9072.
[44] S.J. Freakley, J. Ruiz-Esquius, D.J. Morgan, The X-ray photoelectron spectra of Ir, IrO2 and IrCl3 revisited, Surf. Interface Anal. 49 (2017) 794–799.
[45] D.J. Morgan, Resolving ruthenium: XPS studies of common ruthenium materials, Surf. Interface Anal. 47 (2015) 1072–1079.
[46] M. Chourashiya, R. Sharma, S.M. Andersen, Accurate determination of catalyst loading on glassy carbon disk and its impact on thin film rotating disk electrode for oxygen reduction reaction, Anal. Chem. 90 (2018) 14181–14187.
[47] R. Sharma, M.A. Karlsen, P. Morgen, J. Chamier, D.B. Ravnsbæk, S.M. Andersen, Crystalline disorder, surface chemistry, and their effects on the oxygen evolution reaction (OER) activity of mass-produced nanostructured iridium oxides, ACS Appl. Energy Mater. 4 (2021) 2552–2562.
[48] I.A. Khan, P. Morgen, R. Sharma, S.M. Andersen, Limitations of chronopotentiometry test protocols for stability study on oxygen evolution reaction electrocatalysts and recommendations, J. Phys. Chem. C 128 (2024) 2828–2833.
[49] R. Sharma, Y. Wang, F. Li, J. Chamier, S.M. Andersen, Synthesis of a Pt/C electrocatalyst from a user-friendly Pt precursor (ammonium hexachloroplatinate) through microwave-assisted polyol synthesis, ACS Appl. Energy Mater. 2 (2019) 6875–6882.
[50] A.W. Hull, X-ray crystal analysis of thirteen common metals, Phys. Rev. 17 (1921) 571.
[51] A.H. Reksten, A.E. Russell, P.W. Richardson, S.J. Thompson, K. Mathisen, F. Seland, S. Sunde, Strategies for the analysis of the elemental metal fraction of Ir and Ru oxides via XRD, XANES, and EXAFS, Phys. Chem. Chem. Phys. 21 (2019) 12217–12230.
[52] O. Khalid, T. Weber, G. Drazic, I. Djerdj, H. Over, Mixed RuxIr1–xO2 oxide catalyst with well-defined and varying composition applied to CO oxidation, J. Phys. Chem. C 124 (2020) 18670–18683.
[53] B.E. Hayden, Particle size and support effects in electrocatalysis, Acc. Chem. Res. 46 (2013) 1858–1866.
[54] B. Pang, S. Feng, Y. Xu, H. Chen, J. Li, Y. Yuan, X. Zou, X. Tian, Z. Kang, Ru doped Ir nanowires for high-efficient and durable proton exchange membrane water electrolyzers, Adv. Funct. Mater. (2024) 2411062.
[55] J. Xu, Z. Lian, B. Wei, Y. Li, O. Bondarchuk, N. Zhang, Z. Yu, A. Araujo, I. Amorim, Z. Wang, Strong electronic coupling between ultrafine iridium–ruthenium nanoclusters and conductive, acid-stable tellurium nanoparticle support for efficient and durable oxygen evolution in acidic and neutral media, ACS Catal. 10 (2020) 3571–3579.
[56] J. Li, G. Wu, Z. Huang, X. Han, B. Wu, P. Liu, H. Hu, G. Yu, X. Hong, Vertically stacked amorphous Ir/Ru/Ir oxide nanosheets for boosted acidic water splitting, J. Am. Chem. Soc. Au 4 (2024) 1243–1249.

[57] A. Zagalskaya, I. Evazzade, V. Alexandrov, Ab initio thermodynamics and kinetics of the lattice oxygen evolution reaction in iridium oxides, ACS Energy Lett. 6 (2021) 1124–1133.
[58] S. Geiger, O. Kasian, A.M. Mingers, S.S. Nicley, K. Haenen, K.J. Mayrhofer, S. Cherevko, Catalyst stability benchmarking for the oxygen evolution reaction: the importance of backing electrode material and dissolution in accelerated aging studies, ChemSusChem 10 (2017) 4140–4143.
[59] Z.-Y. Wu, F.-Y. Chen, B. Li, S.-W. Yu, Y.Z. Finfrock, D.M. Meira, Q.-Q. Yan, P. Zhu, M.-X. Chen, T.-W. Song, Non-iridium-based electrocatalyst for durable acidic oxygen evolution reaction in proton exchange membrane water electrolysis, Nat. Mater. 22 (2023) 100–108.